Smart Structures and Systems, *Vol. 33, No. 6 (2024) 399-414*
https://doi.org/10.12989/sss.2024.33.6.399

Long-term shape sensing of bridge girders using automated ROI extraction of LiDAR point clouds

Ganesh Kolappan Geetha [1a], Sahyeon Lee [2b], Junhwa Lee [3c] and Sung-Han Sim[*4]

[1] *Department of Mechanical Engineering, Indian Institute of Technology Bhilai, India*
[2] *Digital Convergence Research Division, Korea Expressway Corporation Research Institute, Republic of Korea*
[3] *Department of Civil Engineering, Pukyong National University, Republic of Korea*
[4] *Department of Global Smart City, Sungkyunkwan University, Republic of Korea*

(*Received November 8, 2023, Revised May 29, 2024, Accepted July 22, 2024*)

Abstract. This study discusses the long-term deformation monitoring and shape sensing of bridge girder surfaces with an automated extraction scheme for point clouds in the Region Of Interest (ROI), invariant to the position of a Light Detection And Ranging system (LiDAR). Advanced smart construction necessitates continuous monitoring of the deformation and shape of bridge girders during the construction phase. An automated scheme is proposed for reconstructing geometric model of ROI in the presence of noisy non-stationary background. The proposed scheme involves (i) denoising irrelevant background point clouds using dimensions from the design model, (ii) extracting the outer boundaries of the bridge girder by transforming and processing the point cloud data in a two-dimensional image space, (iii) extracting topology of pre-defined targets using the modified Otsu method, (iv) registering the point clouds to a common reference frame or design coordinate using extracted pre-defined targets placed outside ROI, and (v) defining the bounding box in the point clouds using corresponding dimensional information of the bridge girder and abutments from the design model. The surface-fitted reconstructed geometric model in the ROI is superposed consistently over a long period to monitor bridge shape and derive deflection during the construction phase, which is highly correlated. The proposed scheme of combining 2D-3D with the design model overcomes the sensitivity of 3D point cloud registration to initial match, which often leads to a local extremum.

Keywords: automated ROI extraction; displacement monitoring; full-scale bridge girder; hough transform and edge extraction; LiDAR-based point clouds; long-term shape sensing

1. Introduction

Dense three-dimensional (3D) point clouds generated by laser scanners or multi-view photogrammetry have significant applications in autonomous driving (Li *et al*. 2020), robotics (Yang *et al*. 2022), remote sensing (Wang and Menenti 2021), Structural Health Monitoring (SHM), and safety assessment (Napolitano *et al*. 2019). Fast and seamless measurements and non-contact reconstruction of 3D structures have numerous applications in SHM (Xu and Stilla 2021). Noteworthy SHM applications for civil infrastructure include dimensional quality assessment of precast concrete (Kim *et al*. 2016), surface feature extraction (Kim *et al*. 2015, 2021a, b), concrete surface crack identification using image processing and deep learning (Kolappan Geetha and Sim 2022, Kolappan Geetha *et al*. 2023), deflection monitoring and shape sensing (Lee *et al*. 2019, Cha *et al*. 2019, 2020, Park *et al*. 2007, Gordon and Lichti 2007), 3D surface reconstruction from Multiview hotogrammetry (Hu *et al*. 2021, Pan *et al*. 2019), and classification of bridge components (Kim *et al*. 2020, Lee *et al*. 2021, Xia *et al*. 2022). Long-term bridge deflection monitoring and deflection model reconstruction with point clouds during the construction phase of a full-scale bridge have not been extensively reported and require much attention.

Cho *et al*. (2018) provided a holistic review of the contact and non-contact sensing schemes for bridge deflection monitoring. Although computer vision-based sensing involving two-dimensional (2D) images (Lee *et al*. 2017, 2020a, b) and multiview photogrammetry (Nocerino *et al*. 2020, Colombani and Andrawes 2022) are cost-effective solutions for non-contact bridge deflection monitoring, they have numerous limitations for bridge model reconstruction. (i) The accuracy of surface reconstruction is primarily affected by ambient lighting conditions and color or texture of the target surface, which is specifically questionable for full-scale field applications. (ii) Computer vision-based sensing often requires the undesirable additional mounting of reference targets in the test structure. (iii) Long-term sensing schemes require customized fixed location mounting attachments to enable time-invariant measurements, which is not feasible for in situ monitoring of construction. (iv) The displacement estimated using multi-view photogrammetry involving Structure From Motion (SFM) and Simultaneous

*Corresponding author, Ph.D., Professor,
E-mail: ssim@skku.edu
[a] Ph.D., Assistant Professor
[b] Ph.D., Researcher
[c] Ph.D., Assistant Professor

ISSN: 1738-1584 (Print), 1738-1991 (Online)

Localization And Mapping (SLAM) is usually in the order of a few tens of millimeters (Wang *et al*. 2020). This accuracy is far from the desired measurement range, making it unsuitable for long-term deformation monitoring or shape sensing. (v) In addition, invariant feature matching for 3D reconstruction in SFM and SLAM is context-specific, and performance accuracy is subjective to test conditions (Wang *et al*. 2020). Although researchers have explored the possibility of relatively inexpensive 3D RGB-D cameras for non-contact SHM (Kim *et al*. 2021a, b, Lee *et al*. 2020a, b) of the target structure, the limitations discussed above persist.

3D point clouds generated using laser scanners are a viable option for long-term displacement measurements (Lee *et al*. 2019, Cha *et al*. 2020) and shape sensing (Cha *et al*. 2019, Park *et al*. 2007), thereby overcoming the limitations discussed previously. These scanners have garnered significant attention in recent years in remote sensing, architecture, engineering, and construction industry. They measure the 3D geometric coordinates of the target structure in a local coordinate system and enable the creation of a geometric model of the measured Region Of Interest (ROI). The scanning head in the Terrestrial Laser Scanners (TLS) rapidly measures the entire 360° with a seamless number of 3D coordinates to generate a wealth of spatial information termed as a 'point cloud'. The scanning head rapidly rotates along horizontal and vertical directions, and extracts distance, azimuth and altitude of the target with respect to the laser scanner. The scanning head records the azimuth and altitude of the projected laser beam as it rotates, and the distance is measured using Time-Of-Flight (TOF) or phase-shift. A comprehensive discussion of the measurement physics (TOF and phase-shift) for laser scanners and types of laser scanners (airborne, TLS or LiDAR, mobile, and robotic) used in a variety of domains is provided in the literature (Rutzinger *et al*. 2009, Di-Stefano *et al*. 2021, Sohn and Park 2021, Royo and Ballesta-Garcia 2019) and references therein. The backscattered laser intensity from the target surface is a direct measure of the local surface reflectance that distinguishes different terrains of surfaces. Tan and Cheng (2016a, b), Tan *et al*. (2019) used calibration studies to distinguish different types of surfaces based on surface reflectance, which was estimated from the peak amplitude of the backscattered intensity. A reflectance-based approach for segmenting components of full-scale bridges is not feasible due to the constraints on independent calibration of control parameters, such as the range and orientation of LiDAR, separately.

The measured dense point cloud includes background vegetation, non-stationary background during construction, multiple bridge girders, supporting structures, and adjacent structures. Hence, long-term shape sensing requires an efficient and automated scheme for extracting point clouds in the ROI. The ROI is application-specific, which may include the entire target structure or part of it. Reported approaches for full-scale bridge deflection monitoring using TLS employ retro-reflective points for measurements, which require tedious surface preparation and manual mounting (Lee *et al*. 2019). This approach is context-specific and not feasible for all bridges. In this study, the ROI consisted of a bridge girder and abutments. Manual segmentation of the ROI from a full-scale bridge girder in a noisy nonstationary background during the construction phase is time-consuming and labor-intensive. Additionally, TLS is a sensitive and costly sensor that cannot be deployed continuously in the field for a long duration due to the security and ambient conditions at the construction site; hence, a scheme invariant to the coordinate measurement system is required for ROI extraction and change detection. To overcome this limitation, Cabaleiro *et al*. (2020) used removable spheres as reference targets on the ROI to transform point clouds into a common reference frame. The computation of the transformation matrices using reference targets on ROI is questionable as the load-carrying ROI induces elastic deformation, which is unaccounted for in Cabaleiro *et al*. (2020). Additionally, automated extraction of the centroid of point clouds on a spherical surface is subjected to error and often requires manual intervention. In the present work, pre-defined flat targets placed in the abutments were used to extract transformation matrices, which are assumed to be rigid.

The literature provides a thorough discussion on 3D data registration, which involves transforming point clouds through rotation, translation, and scaling into a common reference frame. This process is particularly relevant for detecting deformation in full-scale rail, road, and highway bridges (Graves *et al*. 2022, Liu *et al*. 2020, Oskouie *et al*. 2016, Ye *et al*. 2018, Ziolkowski *et al*. 2018). Notable limitations in implementing 3D registration for point-to-point matching are as follows: (i) 3D registration is sensitive to initial match configuration and typically requires a manual alignment with multiple pairs of common points, followed by fine alignment. (ii) In certain scenarios, multiple iterations of manual registration are necessary to achieve minimal errors. (iii) The accuracy of the planar registration in (Liu *et al*. 2020) is constrained by the accuracy of the feature point recognition. (iv) For photogrammetry (Graves *et al*. 2022, Melo *et al*. 2020), the registration error is highly sensitive not only to optical illumination parameters but also to the extrinsic parameters of camera calibration. Recently, alternate approaches using deep learning have been employed for automated structural component extraction (Kim *et al*. 2021a, b) and deterioration monitoring (Gharehbaghi *et al*. 2022). Kim *et al*. (2021a, b) reported an automated segmentation scheme to distinguish point clouds using subspace partition and deep learning. The limitations of (Kim *et al*. 2021a, b) are summarised as follows: (i) the requirement of a large dataset for deep learning (DL)-based training and testing (ii) the accuracy of segmentation and its overlap with the adjacent component is dependent on the subspace length (iii) full-scale bridge girders involve numerous labeled classes (iv) labeling is labor-intensive and time-consuming. Recently, Truong-Hong and Lindenbergh (2022) and Lu *et al*. (2019) extracted the surface point clouds of the bridge surface using contextual knowledge in a consecutive sequence from the superstructure to substructure. Yan and Hajjar (2021) proposed the segmentation of point clouds on bridges wherein knowledge of geometry, topology, and spatial relationship are modelled and implemented based on

a heuristic method. However, these approaches require manual tuning of empirically chosen parameters that satisfy global and local geometric variations. The authors of this paper overcome the limitations discussed above by developing an automated approach that combines 2D-3D methods of image processing and surface fitting along with the design model and pre-defined targets for ROI extraction (Schnabel *et al*. 2007, Torr and Zisserman 2000).

The reported literature (Cha *et al*. 2019, 2020, Park *et al*. 2007) on shape sensing, which is closely related to bridge SHM, has been limited to lab-scale testing and controlled field experiments. These findings are not applicable for full-scale bridge girder monitoring for the following reasons: (i) A precise definition of the bridge component ROI is not feasible during the construction phase. (ii) Point clouds measured from field experiments include the surrounding nonstationary background and vegetation. (iii) In case of lab-scale testing, experiments are often performed on a scaled representative specimen of the target structure, where the span of the specimen is scaled. Hence, the relative range and angular parameters for LiDAR measurements between the extremes of scaled specimen are relatively constant or small, which may not hold true for full-scale bridges. (iv) Field experiments contain noisy point cloud outliers due to irregular local reflectivity from the target surface. (v) Mixed pixels and occlusion effects from temporary structures are present during bridge construction. (vi) In field experiments, the TLS cannot be continuously deployed at the construction site. To overcome this, surveyors employ setting up a network with reference prisms. Ideally, these reference prisms should be positioned outside the zone of ROI and be equally distributed around the measurement sensing unit at similar angles. However, this can be a cumbersome task as it requires ensuring a clear line-of-sight in the presence of movable background. In addition, the data and computational complexity of automated ROI extraction and resolution effects have not been well explored in the context of full-scale bridge inspection.

To overcome these limitations a scheme is proposed for long-term shape sensing and deformation monitoring of full-scale bridges using point clouds with automated extraction of ROI invariant to LiDAR positions. This scheme combines design information with 3D surface fitting and 2D image processing to extract point clouds in the ROI and reconstruct a geometric model for shape sensing and deformation monitoring. The rest of the paper is organized as follows: the algorithm for automated ROI extraction and long-term shape sensing is discussed in Section 2. Here, details about the point clouds acquisition and test bed details, topology extraction of pre-defined targets using Otsu-based threshold scheme, boundary extraction using an image-based approach, and in-plane and out-of-plane registration using pre-defined reference targets are presented. This section also summarises optimal deformation profile reconstruction using least-squares-based shape sensing. In Section 3, long-term shape sensing and deformation monitoring results from full-scale bridge girder are discussed with the investigation for measurement-related uncertainties. The study is concluded in Section 4 and the limitations as well as future directions are discussed.

2. Automated ROI extraction and shape sensing of a full-scale bridge girder

The proposed methodology enables long-term shape sensing and deformation monitoring, wherein an efficient automated ROI extraction scheme that is invariant to the LiDAR position is employed. Automated ROI extraction reconstructs a geometric model, wherein 2D and 3D methods are combined along with the design model and pre-defined targets for ROI extraction. The methodology developed in this study extracts and transforms the ROI from different dated measurements in the LiDAR coordinate system into a unified world coordinate system, thereby enabling long-term shape sensing and deformation monitoring. Fig. 1 presents an overview of the proposed automated ROI extraction and long-term shape sensing framework.

The procedure shown in Fig. 1 was designed to enable long-term deflection monitoring of bridges using point cloud data. It consists of six steps: point cloud acquisition, preprocessing, boundary pixel extraction, in-plane transformation, out-of-plane transformation extraction and ROI extraction, and long-term shape sensing. The details of each step are as follows:

2.1 Point cloud acquisition and experimental test bed details

Field experiments were performed for long-term shape sensing on a full-scale concrete railroad bridge (Fig. 2(a)) (Lee *et al*. 2019), where the point clouds were measured during different phases of bridge construction. Different dated point clouds were acquired in the LiDAR coordinate system (X_T, Y_T, Z_T), which is a typical form of long-term measurements. The bridge includes four prestressed concrete girders, whose dimensions are shown in Fig. 2(b) (Lee *et al*. 2019). Point cloud measurements were obtained using a Riegl VZ-1000 laser scanner that uses a near-infrared laser with a constant pulse repetition rate. The horizontal and vertical scan spatial resolutions were 0.001° (equivalent spatial resolution of 0.35 mm for a 20 m distance) and 0.006° (2.09 mm for a 20 m distance). The major dimensions of the bridge girder, such as the span and width of a single bridge girder, were 40 and 2 m, respectively. The laser scanner was placed under the mid-span of the bridge. Two retroreflectors, referred as 'reference reflectors' each with a 50 mm diameter, were affixed to each abutment for coordinate transformation. Since the abutments of the bridge girder are assumed to be rigid, and bearings are provided on top of abutments to account for dynamic loads, elastic deformation can be negligible or minimal, indicating that the position of retroreflectors can be assumed to remain constant during long-term monitoring. The 3D point cloud measurements for a full-scale bridge girder with TLS involve two scanning levels. Coarse grid scanning was performed for global measurements, followed by high-resolution dense scanning of the area around the reflector. Reflectors are small and thin with replaceable attachments with retroreflective

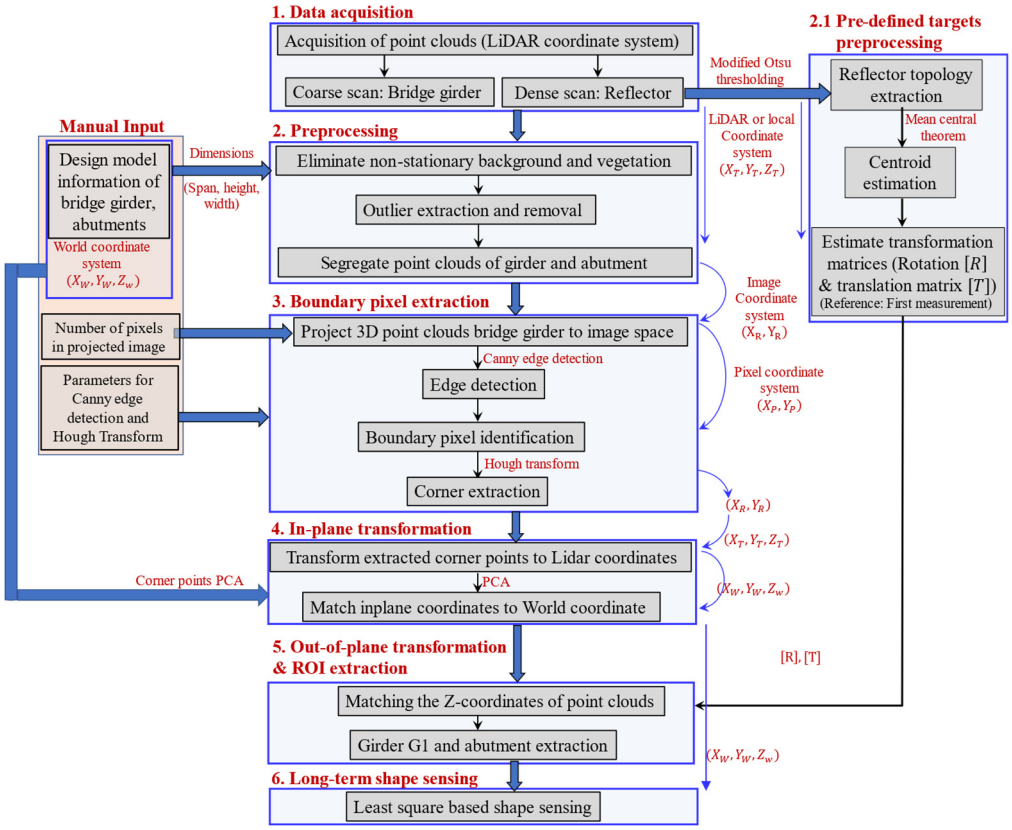

Fig. 1 Flow chart illustrating long-term shape sensing with automated ROI extraction involving transformation across multiple coordinate systems

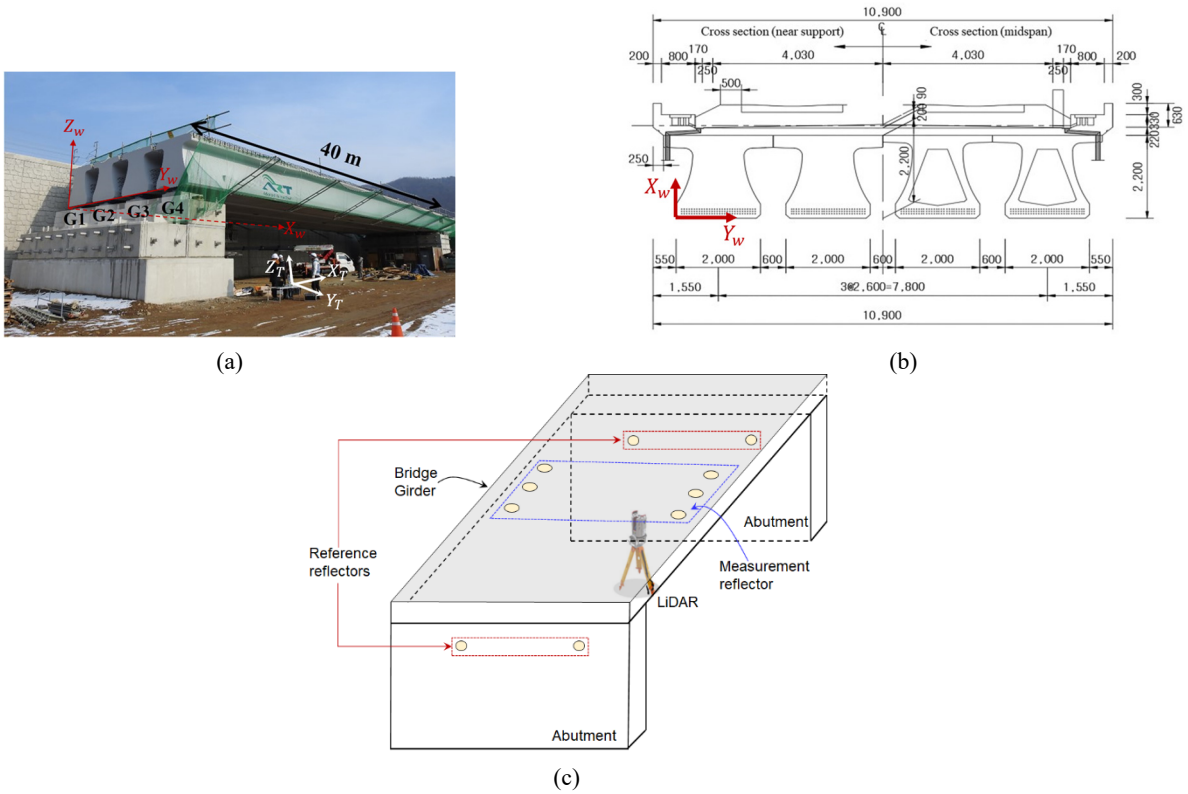

(a) (b) (c)

Fig. 2 (a) Full-scale concrete railroad bridge during construction phase (Lee *et al*. 2019). (b) Dimensions of bridge girder cross-section; all dimensions are in mm (Lee *et al*. 2019). (c) Schematic showing bridge girder, 'measurement and reference reflectors', and location of LiDAR

coatings mounted on the bridge abutments to provide additional information during measurements. To obtain the ground truth measurement of bridge deflection, six retroreflective reflectors called 'measurement reflectors' are symmetrically placed around the mid-span of the bottom surface of bridge girder G1 (Fig. 2(c)). The point clouds from the measurement reflectors are projected onto the gravity vector to compute the mid-span deflection. Symmetrically attached measurement reflectors provide the best approximation of the gravity vector at the mid-span. On each measurement day, the LiDAR is repositioned, and measurements are obtained on both the reference and measurement reflectors in the same LiDAR coordinate system. The position information of reference reflectors in each measurement set is used to transform measurements from measurement reflectors to the world coordinate system. A detailed discussion of the experimentation for long-term displacement measurement of bridges using LiDAR system is discussed in Lee *et al*. (2019).

The current study utilized point clouds obtained from a single scanning station. However, when surveying larger bridges, multiple scanning stations may be utilized to cover a larger field of view. Point clouds from multiple scanning stations can be stitched using planar and/or vertical registration of point clouds using conventional surface feature points. However, these approaches are constrained by the accuracy of the feature point recognition.

2.2 Preprocessing

The raw point cloud (x_i, y_i, z_i) measured in the LiDAR coordinate system (X_T, Y_T, Z_T) (Fig. 3(a)) includes surrounding background information such as ground points, vegetation, non-stationary background during construction, and adjacent structures. The color intensity scale in Fig. 3(a) represents the reflectance amplitude calibrated against an reference sample, whose details are not provided by Original Equipment Manufacturer (OEM) of the LiDAR equipment. In the current study, the ROI was the bridge girder G1 (see Fig. 2(a)) and corresponding abutments. The background point clouds were filtered using the following design information.

$$\sqrt{(x_i - X_T)^2 + (y_i - Y_T)^2 + (z_i - Z_T)^2} < 0.75L_{\text{span}};\quad 0.25H_{\text{girder}} < (y_i - Y_T)^2 < 1.5H_{\text{girder}} \tag{1}$$

where (x_i, y_i) and z_i are the in-plane and out-of-plane coordinates of the i$^{\text{th}}$ point cloud, respectively. L_{span} and H_{girder} are the span and height of the bridge girder, respectively, obtained from the design information. Using Eq. (1), a major portion of the vegetation and ground points was filtered, and the four girders and abutments are shown in Fig. 3(b).

The rule-based thresholds $0.75L_{\text{span}}$ and $0.25H_{\text{girder}}$ in Eq. (1) are chosen from a conservative perspective to filter outlier point clouds. For a point cloud data set of approximately one million points, conservative thresholds of 25% on the length and span of the bridge girder filter a large fraction of the outlier point cloud at the preliminary step, thereby reducing associated computational complexity in the subsequent steps. For a tighter threshold on the length and span of the bridge girder, a high density of point cloud measurement is needed to avoid false outliers. However, in our current approach, we adopted a coarse point measurement globally, followed by high-resolution dense measurements at the region of reference reflectors. 25% threshold on the height filters are large ground points from the point cloud dataset. Often in the context of point clouds, it's a trade-off between accuracy, measurement time, false classifiers/outliers, and computational complexity.

The next step involved removing the points out of ROI that exhibited significant variation in the z-coordinate values, which were measured from the bottom surface of the girder. This was achieved by utilizing the state-of-the-art modified RANSAC (MSAC) algorithm on the background-filtered point cloud (Torr and Zisserman 2000). The inlier point clouds extracted by MSAC were used to an approximate plane with a maximum allowable distance from inlier points to the plane. The plane-fitting scheme uses a pre-defined threshold derived as follows. First, the mean Z_T coordinate values (Z_{mean}) from the bottom surface of the girder point cloud data were determined. The lower $(Z_{\text{min}} = Z_{\text{mean}} - 100S_R)$ and upper bounds $(Z_{\text{max}} = Z_{\text{mean}} + 100S_R)$ of the thresholds were determined by selecting a distance of 100 times (two orders of magnitude) the minimum spatial resolution (S_R) of the point cloud on the target structure. The approximate fit plane was insensitive to the maximum allowable distance ranging from $20S_r$ to $200S_r$ meters. All point clouds below the fitted plane were separated to isolate the bridge girder from the abutments. Fig. 4(a) shows the surface-fitted girder region with an adjacent boundary wall near G1. Surface filtering eliminates point clouds that are beyond bounds. Cross-sectional views showing the upper and lower bounds of the threshold and filtered point clouds are shown in Figs. 4(b) and (c), respectively. Although many outliers

(a) (b)

Fig. 3 (a) Raw point cloud and (b) background filtered point cloud showing the ROI of the bridge girder

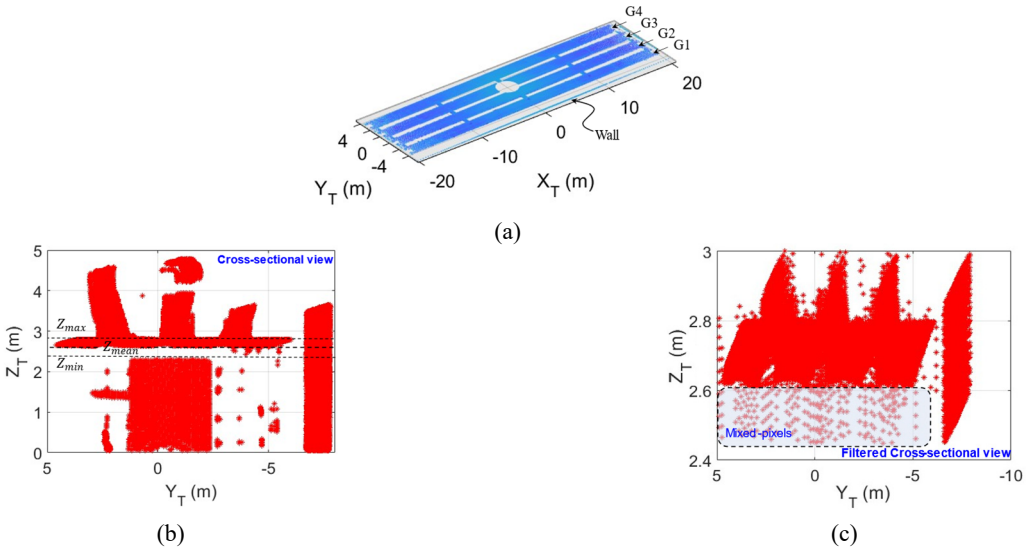

(a) (b) (c)

Fig. 4 (a) The extracted girder plane after surface fitting. (b) Threshold bounds mapped on the cross-sectional view for the plane fitting. (c) Isometric view showing filtered point clouds using the threshold bounds

were removed using the proposed approach, the mixed pixel phenomenon is one of the limitations of point clouds generated using laser scanners (see Fig. 4(c)). At the corner or edge region, the laser beam splits into two and reaches two distinctive surfaces involving different 3D surfaces. The encoders in the laser scanner receive two different range measurements, causing inaccuracies. Hence, around the edge region (Fig. 4(c)), non-coherent point clouds are observed, which are outliers that are eliminated during optimal deformation profile-based shape sensing.

2.2.1 Conventional point cloud registration

From the perspective of a bridge surveyor, non-target-based conventional point cloud registration is convenient, as discussed in Graves *et al*. (2022), Liu *et al*. (2020), Oskouie *et al*. (2016), Ye *et al*. (2018), Ziolkowski *et al*. (2018). However, these approaches often require multiple iterations of manual alignment to minimize the registration errors, which makes the automation of long-term shape sensing and deformation monitoring of bridge girder difficult. As conventional 3D point cloud registration is sensitive to initial match configuration, a two-step process is often implemented, where an initial manual alignment precedes an iterative closest point algorithm-based point-to-point matching. Fig. 5 shows superposed point clouds measured from two different LiDAR positions (a) before and (b) after conventional 3D registration without manual iteration. Although the error between point-to-point matching from the conventional 3D registration is minimal, local convergence is reached instead of global convergence due to the sensitiveness of the initial configuration. This is observed in Fig. 5(b), where after 3D registration point clouds of bridge girder ‘G1’, ‘G2’, ‘G3’ (blue color data set) matches with point clouds of ‘G2’, ‘G3’, ‘G4’ (red color data set), respectively. These errors cumulatively accumulate in subsequent computation. This limitation for long-duration shape sensing and deformation monitoring is overcome by using pre-defined targets for registration.

2.2.2 Topology extraction of pre-defined targets

Reflectors are small and thin replaceable attachments with a retro-reflective coatings mounted on the target structure to provide additional information during measurements (Fig. 2(a)). High-resolution dense 3D point cloud measurements in the ROI of reflectors are more accurate, with a high signal-to-noise ratio. In the present

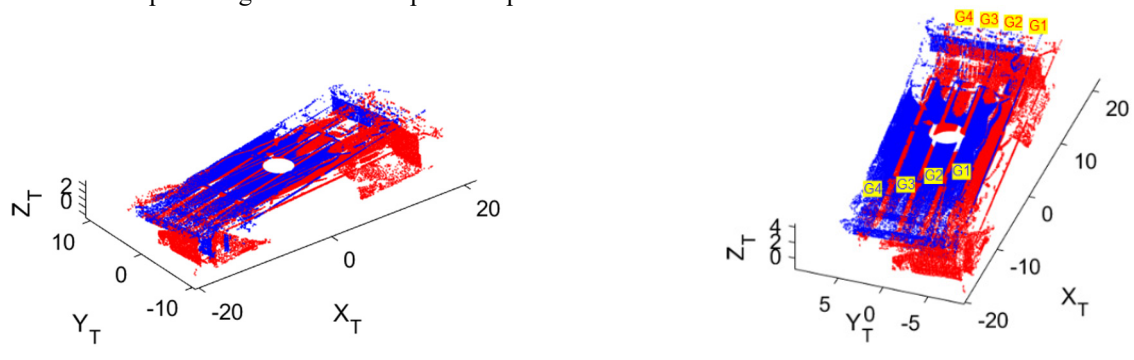

(a) (b)

Fig. 5 Superposing point clouds measured from two different LiDAR positions (a) before and (b) after conventional 3D registration

context, the extraction of reflector topology aids in constructing the translation $[t]$ and rotation $[R]$ components for transforming the extracted point clouds from the LiDAR coordinate system to the world coordinate system. The point clouds obtained in the ROI of the reflectors include information about the 3D coordinates and reflected intensity from the reflector patch. The reflector region has a high reflectivity compared to the background. Thereby the reflector topology can be distinguished from the surrounding background by deriving the reflectance intensity of the point cloud in the ROI (Fig. 6(b)).

Automated global thresholding schemes based on the reflectance intensity, such as (i) the Otsu method (Otsu 1979) (ii) the valley emphasis Otsu threshold (Ng *et al*. 2013) (iii) entropy-based Otsu threshold (Truong and Kim 2018) separate the topology of the reflectors. Although Lee *et al*. (2019) used an automated Otsu-based thresholding on the reflectance intensity segregate the reflector topology, the accuracy of the extracted topology is questionable because the reflectance histogram is unimodal or close to a unimodal distribution (Fig. 6(b) and Fig. 7). The locations of the TLS are not the same for each measurement because of unforeseen difficulties during the construction phase. The extracted reflector topology through various thresholding schemes is not accurate in all instances; hence, a unified approach works consistently for all measurements and orientations of the TLS.

The various automated threshold extraction schemes are summarized as follows: for an interval $[0, L-1]$ using discriminant analysis, following the standard notation (Otsu 1979), the optimal Otsu threshold (t^*) is given by

$$t^* = \text{Arg} \max_{0<t<L-1} \{(P_0(t)\mu_0^2(t) + P_1(t)\mu_1^2(t))\}, \quad (2)$$

where $P_0(t)$ and $P_1(t)$ are the class probabilities of the background and reflector, respectively. $\mu_0(t)$ and $\mu_1(t)$ are the mean values of the classes representing the background and reflector, respectively. The optimal threshold (t^*) for the valley emphasis Otsu threshold (Ng *et al*. 2013) is determined by

$$t^* = \text{Arg} \max_{0<t<L-1} \{(1-h(t))(P_0(t)\mu_0^2(t) + P_1(t)\mu_1^2(t))\}, \quad (3)$$

where the first term $(1-h(t))$ is the weight function. Similarly, the optimal threshold (t^*) for entropy-based Otsu filtering (Truong and Kim 2018) is determined by

$$t^* = \text{Arg} \max_{0<t<L-1} \{\psi(t)\,(P_0(t)\mu_0^2(t) + P_1(t)\mu_1^2(t))\}, \quad (4)$$

where $\psi(t) = \ln t(L-1-t)$. The optimal threshold that works consistently for all measurements and orientations of the TLS by determining the maximum threshold among Eqs. (2), (3), and (4). The representative threshold estimation and reflector shape extraction from the background are shown in Fig. 6 and Fig. 7, respectively. The histogram distribution of the reflectance (Fig. 6(b)) was

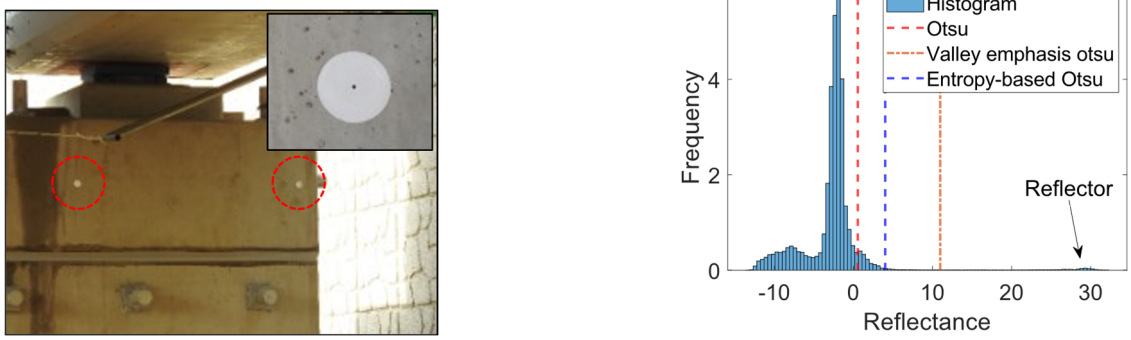

(a) (b)

Fig. 6 (a) Representative image showing ROI of retroreflector attached on a bridge abutment, and (b) the corresponding reflectance histogram

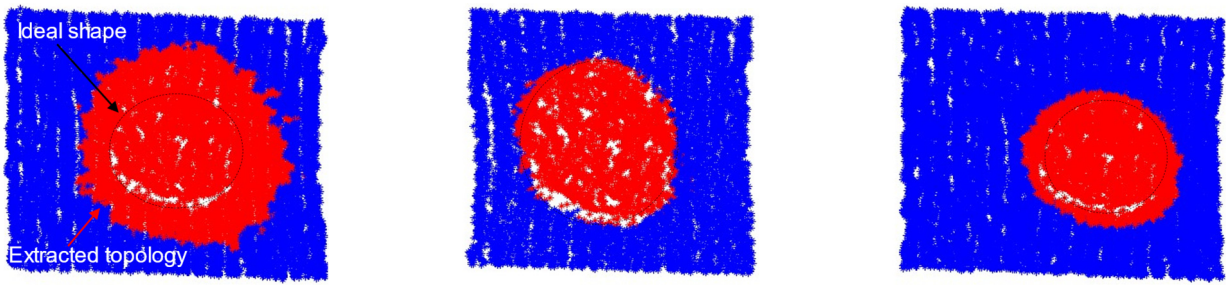

(a) (b) (c)

Fig. 7 Extracting 2D reflector topology from fine resolution LiDAR scan (Fig. 6(a)) using different thresholding methods: (a) the Otsu method, (b) Valley emphasis Otsu threshold, and (c) Entropy-based Otsu threshold

close to unimodal distribution for the representative image shown in Fig. 6(a). The maximum threshold corresponds to the valley between the reflector and background reflectance histogram, indicating the optimal extraction of reflector topology among various thresholding schemes. For the representative image shown in Fig. 6(a), the maximum threshold obtained using the valley-emphasis Otsu method provided the optimal reflector topology (Fig. 7(b)). Furthermore, the 3D centroid was estimated from the extracted reflector topology using the mean central limit theorem (Durrett 2019) to transform the point clouds from the LiDAR coordinate system to the world coordinate system. The output comprises the 3D coordinates of the centroids of four pre-defined targets that are mounted on the abutments.

2.3 Boundary pixel extraction in 2D image space

After separating the background filtered bridge girders and abutments, the 3D point clouds of bridge girders (Fig. 4(a)) are projected onto 2D image space (X_R, Y_R) plane fitted using point clouds. First, the 3D point clouds in the X_T and Y_T coordinates are subdivided using a user defined spacing. The span of the X_R and Y_R coordinates was determined based on the maximum and minimum values of the point clouds. Next, all the point clouds belonging to each sub-grid or cell were assigned common $X_{i,j_{\text{centroid}}}$ and $Y_{i,j_{\text{centroid}}}$ values, corresponding to the centroidal values of each cell, and a mean average $Z_{i,j_{\text{centroid}}}$ value of the point clouds in that cell was assigned. For each cell with a valid $Z_{i,j_{\text{centroid}}}$ value, the values computed as $\sqrt{X_{i,j_{\text{centroid}}}^2 + Y_{i,j_{\text{centroid}}}^2 + Z_{i,j_{\text{centroid}}}}^2$ were assigned and normalized with the maximum value among all grids. Each grid corresponds to single pixel in the projected image. In the current work, the dimensions of each grid were approximately $100S_R$ meters times (two-orders of magnitude) the spatial resolution of point clouds on bridge girder. The results were insensitive to the choice of grid size ranging from a factor of $20S_R$ to $200S_R$ meteres.

The edges of the bridge girder were extracted from the 2D projected image using Canny edge detection (Hough 1962) (Fig. 8(b)). The lower and upper threshold for Canny edge detection was 0.01 and 0.05, respectively. The normalized value of edge pixels above the upper threshold (0.15) are considered and below the lower threshold of 0.01 are discarded. Those pixels within the bounds of the lower and upper thresholds are considered only if these pixels are connected to pixels with upper threshold. The intermediate

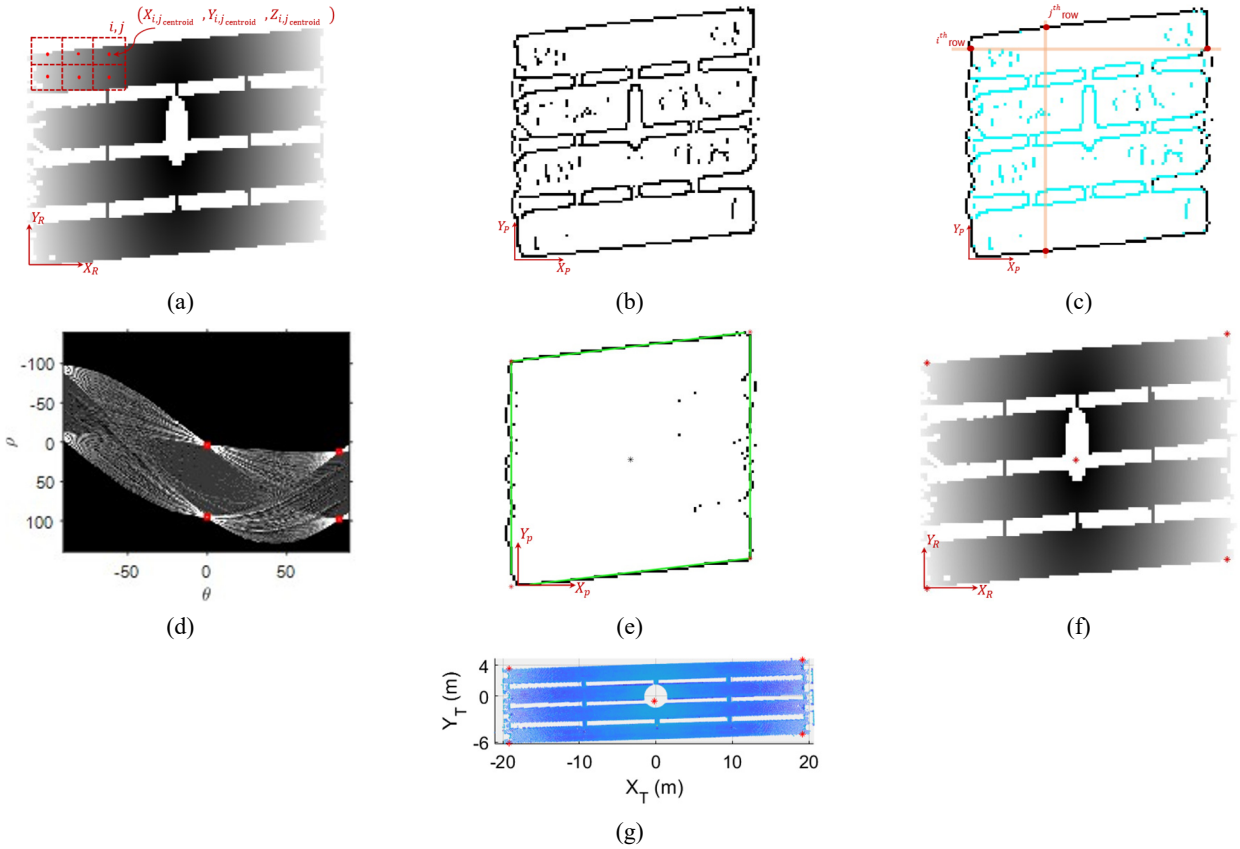

Fig. 8 Steps involved in the image-based approach for extracting boundary coordinates: (a) 3D point cloud projection into 2D space, (b) Canny edge detection, (c) extraction of outer boundary pixels, (d) Hough space representation of boundary pixels, and (e) reconstructed boundary edges, (e)–(g) show the extracted corner points (red markers) in the pixel coordinate system, projected 2D image coordinate system, and the local LiDAR coordinate system. (Note: (X_p, Y_p) represent the pixel coordinate system, (X_R, Y_R) represent the range image space, (X_T, Y_T) represent the LiDAR coordinate system)

edge pixels were filtered out, and only the pixels corresponding to the boundary edges were retained by extracting the first and last pixels along each row and column (see Fig. 8(c)). To extract the boundary corner points from the intersection of edge lines, the extracted edge pixels were transformed into Hough space (Hough 1962), which is an alternate way to represent a line. In the Hough space, the edge pixels are represented as a normal line in the form $\rho = x\cos\theta + y\sin\theta$, in $\rho - \theta$ plane, where ρ represents the length of a normal line and θ denotes the angle between the line and x-axis. Four significant peaks were extracted from the Hough transformation matrix with a minimum threshold of 0.1 times the maximum value. After each peak is identified, a suppression neighborhood threshold of 49 pixels in each direction is set to zero. In the current context, a range of suppression thresholds from 25 to 51 pixels was found to be insensitive for an image of 100×100 pixels. Here, approximately 100 pixels correspond to the span of the bridge girder projected in 2D image. The intersection points extracted from the Hough parameter space (shown in red in Fig. 8(d)) are sequentially transformed through (i) pixel space (Fig. 8(e)), (ii) projected 2D image space (Fig. 8(f)), and (iii) the LiDAR coordinate system (Fig. 8(g)). The accuracy of this method depends on the spatial division during the construction of the range image.

2.4 In-plane coordinate transformation

The extracted corner points in the LiDAR coordinate system (Fig. 8(g)) were used to perform principal component analysis (PCA) to obtain the 2D basis vectors. These basis vectors were then used to match the in-plane coordinates of point clouds with the design coordinates in the unified world coordinate system (X_W, Y_W, Z_W). The difference in the in-plane rotation $(\Delta\theta)$ (Fig. 9(a)) and centroid translation (ΔT) between the world coordinate system and LiDAR coordinate system (Fig. 9(b)) were calculated and the in-plane coordinates of the point clouds were transformed to the design coordinate system. Fig. 9 (b) shows the translated and rotated in-plane point clouds in the world coordinates. The matched point clouds in the world coordinates were combined with the design model information (design dimensions) to extract the point clouds of girder G1 (see Fig. 9(c)). Using the proposed approach, the in-plane coordinates of the different dated measurements were aligned to a unified coordinate system.

2.5 Out-of-plane coordinate transformation and ROI extraction

The optimal rotation and translation matrices employed for matching the out-of-plane coordinates were constructed using the centroids estimated from the extracted reflected (pre-defined targets) topology. The first measurement served as the reference measurement for constructing transformation matrices. The measurements taken during the construction of the full-scale bridge girder in the LiDAR coordinate system were denoted by 'A' for the first time and 'B' for the differently dated time. The minimum number of points required to find the optimal rotation and translational matrix is three. However, in our case, we have centroids from four different reflectors to find the optimal rigid-body transformation matrices. Since there was assumed to be no change in the shape and size of the reflector topology, a rigid-body transformation was considered instead of an affine transform that includes scaling and shearing. The optimal matrices during rigid body transformation were estimated using least-squares errors. Measurements 'A' and 'B' with 'n' point clouds are given as follows

$$[A] = \left[A^{(i)}\right] = \left[A^{(1)}\ A^{(2)}\ \ldots\ A^{(n)}\right]; \quad [B] = \left[B^{(1)}\ B^{(2)}\ \ldots\ B^{(n)}\right] \tag{5}$$

A^i and B^i are 3×1 vectors corresponding to 3D coordinates. The rigid-body transformation is represented as follows

$$[B] = [R][A] + [t] \tag{6}$$

where [R] and [t] are rotational and translational matrices, respectively. The centroid is found by using the mean centroidal theorem, facilitated by obtaining a fine-resolution dense measurement at the location of the reflector. The translational matrix is given as follows

$$[t] = \{C_B\} - [R]\{C_A\} \tag{7}$$

where $\{C_A\}$ and $\{C_B\}$ are the centroid vectors given by

$$\{C_A\} = \left\{\frac{1}{n}\sum_{i=1}^{n} A^{(i)}\right\}; \quad \{C_B\} = \left\{\frac{1}{n}\sum_{i=1}^{n} B^{(i)}\right\} \tag{8}$$

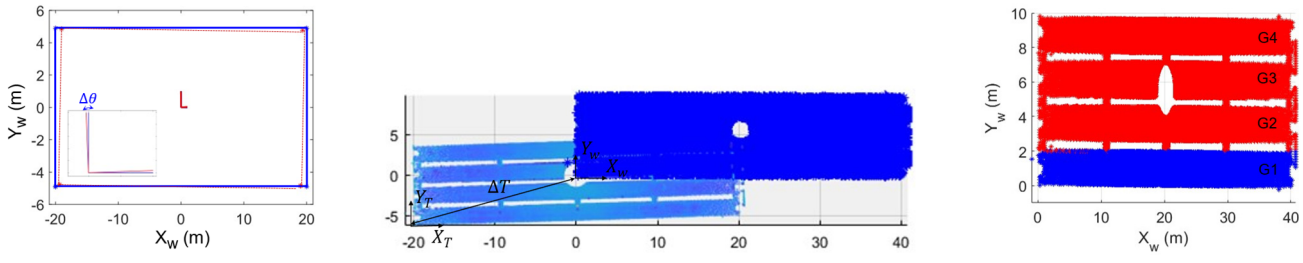

(a) (b) (c)

Fig. 9 (a) Image-based superposition of principal components obtained from the design coordinates system and reconstructed corner points. (b) Rotated and translated point clouds matched with design or unified world coordinate system. (c) Extraction of the bridge girder G1 using design information (blue point clouds) (All dimensions are in m)

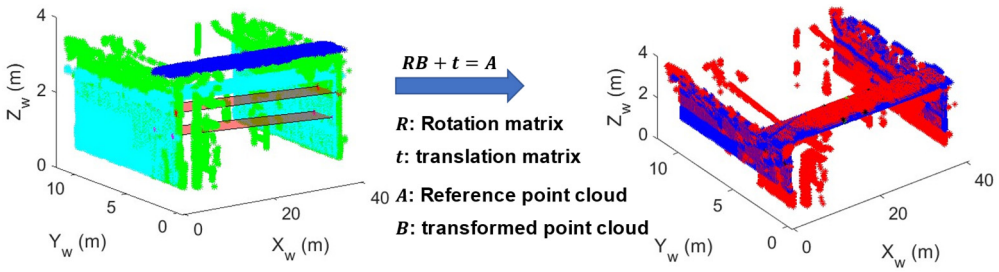

(a) (b)

Fig. 10 Matching out-of-plane coordinates of point clouds from each measurement to a unified world coordinate system (First measurement is the reference in the world coordinate system)

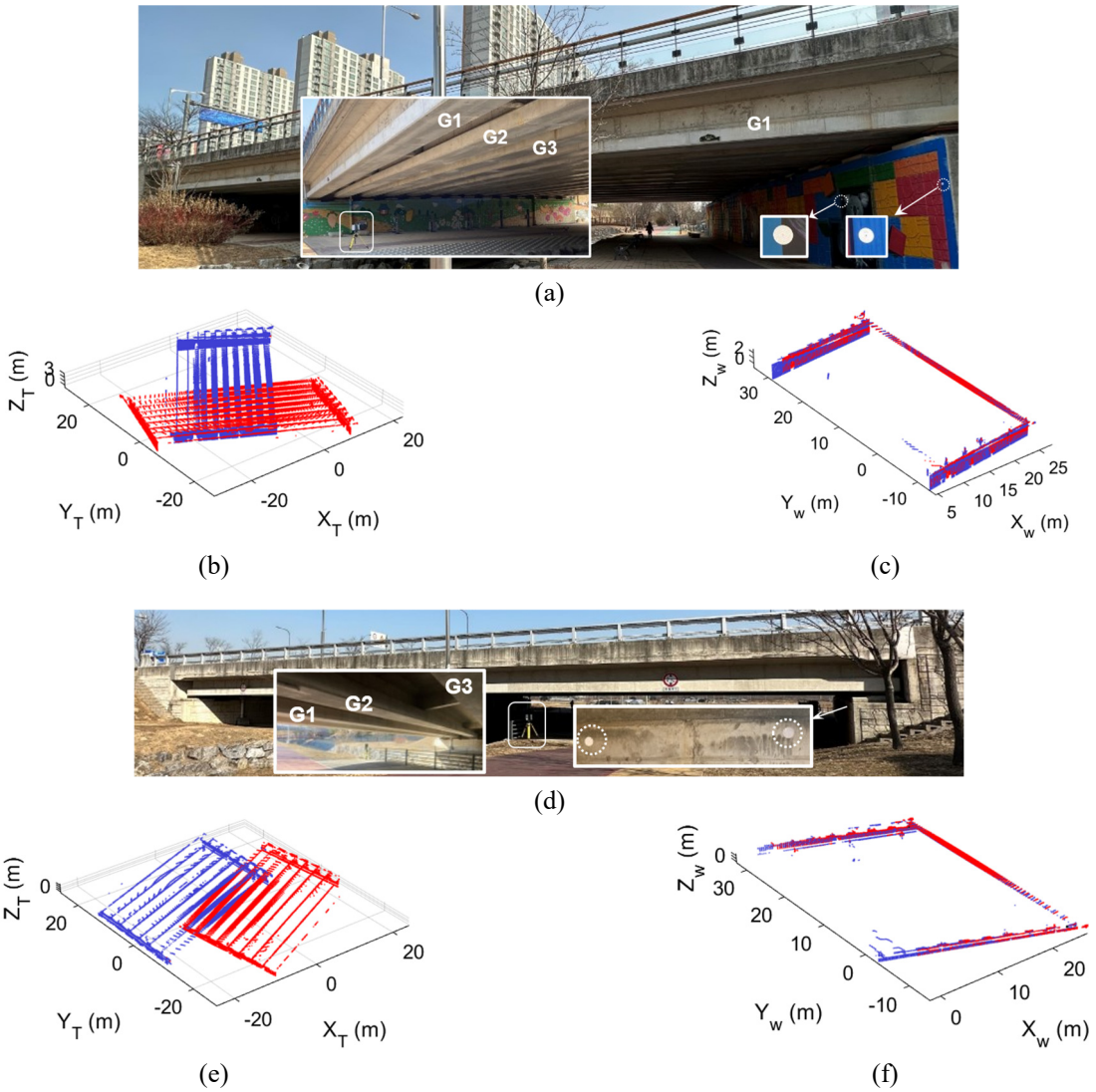

(a) (b) (c) (d) (e) (f)

Fig. 11 (a), (d) Additional case studies on different bridge girders to validate the proposed scheme. Inset within (a) and (d) shows positions of LiDAR and ROI of retroreflector attached on a bridge abutment. (b), (e) The corresponding background filtered point cloud from different positions of LiDAR (X_T, Y_T, Z_T). (c), (f) Point clouds of bridge girder G1 and abutments transformed to a unified world coordinate system (X_W, Y_w, Z_w) from different measurement sets

The translational component is removed as follows

$$[H] = \left[A^{(i)} - C_A\right]\left[B^{(i)} - C_B\right]^T \quad (9)$$

The real-valued covariance matrix $[H] \epsilon \boldsymbol{R}^{n \times m}$ which can be uniquely decomposed as follows

$$[H] = [U][\Sigma][V]^* \quad (10)$$

where $[U]\epsilon\boldsymbol{C}^{n\times n}$ and $[V]\epsilon\boldsymbol{C}^{m\times m}$ are unitary matrices with orthonormal columns and $[\Sigma]\epsilon\boldsymbol{R}^{n\times m}$ is a matrix with real, and non-negative entries on the diagonal and zero off-diagonal elements. The rotation matrix R can be expressed as Strang (2022).

$$[R] = [V][\mathrm{U}]^T \tag{11}$$

The out-of-plane coordinates of the different dated measurements were matched to a single frame of reference using the transformation (rotation and translation) of point clouds corresponding to girder G1 and abutments using the pre-defined reference reflector targets. Further, the girder G4 and abutment were rotated and translated to world coordinates. Fig. 10 shows the successive transformation of the point clouds from the LiDAR coordinate system to the world coordinate system. In the unified world coordinate system (X_w, Y_w, Z_w), the ROI point clouds involving a single bridge girder and abutment were extracted using the design model information. The brown shaded rectangular region in the Fig. 10(a), gives a visual indication of the offset distance between the predefined targets, obtained from two successive measurement sets. The green and cyan color on the Fig. 10(a) indicates two different measurement sets before transforming to unified world coordinate system. The blue color span is used to highlight the contrasting difference between both pairs. The red and blue color in the Fig. 10(a), indicates the transformed point clouds overlayed after matching the coordinates to unified world coordinate system.

The proposed automated ROI extraction scheme, which is invariant to the LiDAR positions on different bridge girders, was validated, as shown in Fig. 11(a) and (d). The spans of bridge girders are 40 m (Fig. 11(a)) and 30 m (Fig. 11(a)), respectively. The height of the bottom surface of the bridge girder from ground level are 3 m and 2.2 m, respectively. The width of the bridge girders is 1.2 m in both the cases. The corresponding filtered point cloud measured from different positions of LiDAR are shown in Figs. 11(b) and (e). The points clouds of G1 were further extracted using design information and they were transformed into a unified world coordinate system (X_W, Y_W, Z_W) (Figs. 11(c) and (f)).

2.6 Long-term shape sensing

After performing 3D registration using pre-defined reference targets, the deformation of the ROI are measured by comparing two sets of point cloud data. Various algorithms for deformation estimation include direct cloud-to-cloud (C2C) distance (Girardeau-Montaut *et al*. 2005), multi-scale model-to-model cloud comparison (M3C2) (Lague *et al*. 2013), and direct point-to-point (P2P) distance metric. The main drawback of the C2C and M3C2 metrics is that neither algorithm establishes exact correspondences between identical locations on the target structure represented by the point clouds. Consequently, the nearest neighbour correspondence for C2C and the mean position correspondence within the core point search volume for M3C2 may not measure the same exact position on the surface of the structure, leading to measurement error. Additionally, these algorithms also struggle in instances where data collection is sparse, leading to potential error and an overall lack of confidence in the results. To address this issue, this paper presents a new distance metric, P2P, which establishes point correspondences via interpolation of point cloud data onto a regularized grid that is shared between the two datasets. However, in the case of P2P, the local surface reflectivity and scanning parameters of point cloud data acquisition plays a significant role in the distance measurement. To overcome these limitations, we reconstructed the optimal deformation profile using least-squares-based shape sensing on the extracted point clouds corresponding to the ROI in the world coordinate system. A non-Lambertian target surface-like concrete introduces significant outliers, which must be smoothed using a robust surface-fitting scheme. The optimal least-squares-based polynomial fitting scheme that is employed in the current framework for the surface fitting of a full-scale bridge girder is concisely summarised following the standard notation (Park *et al*. 2007, Gordon and Lichti 2007). The bottom surface of the considered bridge girder is a plane, and only the fundamental eigenmodes corresponding to bidirectional bending are of interest. The fundamental flexural modes for the considered bridge girder can be approximated using quadratic surface polynomial fitting, given by

$$z_i = a^2x_i^2 + b^2y_i^2 + cx_iy_i + dx_i + ey_i + f, \tag{12}$$

where (x_i, y_i) are the in-plane coordinates and z_i is the transverse bending deformation of the ith point cloud. The compact representation for a system of point clouds is given as follows

$$\{z\} = \begin{Bmatrix} z_1 \\ \vdots \\ z_n \end{Bmatrix} = \begin{bmatrix} x_1^2 & y_1^2 & x_1y_1 & x_1 & y_1 & 1 \\ \vdots & \vdots & \vdots & \vdots & \vdots & \vdots \\ x_n^2 & y_n^2 & x_ny_n & x_n & y_n & 1 \end{bmatrix} \begin{Bmatrix} a \\ b \\ c \\ d \\ e \\ f \end{Bmatrix} = [X]\{\bar{a}\} \tag{13}$$

where $\{\bar{a}\}$ is the surface-fitting coefficient associated with the 2D reconstructed surface. The best fit coefficients of the surface using least-squares fitting are given by

$$\{\bar{a}\} = ([X]^T[X])^{-1}[X]^T\{Z\} \tag{14}$$

Using the estimated surface fitting coefficients, the 2D shape of the girder is reconstructed with a smoothened deformation profile. The surface fitting eliminates the outlier point clouds from each measurement set. Steps outlined above were repeated for each measurement set to obtain the long-term time-dependent deformation profile of the bridge girder. The transformation of point clouds and subsequent shape sensing in invariant unified world coordinates ensures the consistency of the analysis. The reconstructed shapes were compared successively to monitor the shape change over a long period during different stages of bridge construction.

In summary, we proposed a scheme for an automated ROI extraction which is invariant to LiDAR positions. The

proposed approach uses a multi-level measurement scheme, wherein we obtain coarse measurements of the bridge girder and supporting structures (abutment), followed by a dense point cloud of the predefined reference targets. We extract the topology of the pre-defined targets using the modified Otsu method, which accounts for the limitations of unimodal or close to unimodal intensity distribution. The pre-defined reference targets transform the ROI point clouds from the LiDAR coordinate system to a unified world coordinate system. The state-of-the-art 3D registration-based approaches for bridge girders fail to align the point clouds in a common reference frame due to local convergence, which is sensitive to the initial match configuration and often multiple manual iterations are required to achieve minimal errors. In contrast, the proposed approach consistently transforms the point clouds across multiple dimensions and coordinate systems, using both the 3D point cloud and 2D image spaces. Finally, reconstruct the shape of the girder using least-square surface fitting and it is compared with the initial configuration to monitor the shape change.

3. Field test results: Long-term shape sensing

Finally, the 3D deformation shape of the extracted girder was reconstructed using least-squares based shape sensing. Surface fitting with least-squares-based shape sensing eliminates outliers and enables the visualisation of the 2D bidirectional deformation of bridge girder G1 (Fig. 12(a)). The shape change was monitored along mid-width of bridge girder G1 during the different phases of construction (Fig. 12(b)). The shape change provides a direct estimate of the mid-span deflection, which correlates to the maximum allowable deflection and corresponding design life (Fig. 12(c)). The deformation, a derived quantity from shape sensing, is estimated by measuring the relative displacement at the mid-point from the best fit plane reference measurement to the best fit plane of the current measurement. The distances can be quantified either as directional, orthogonal, or relative, depending on the application (Truong-Hong and Lindenbergh 2019). Displacements can also be quantified based on point-to-point, point-to-surface, surface-to-surface, or surface-to-model (Truong-Hong and Lindenbergh 2019). The accuracy of the deformation measurement is subjective to the reference surface, which can be either a surface reconstructed from the first measurement or a design surface/model. In the context of deformation monitoring of the bridge girder during the construction phase, the baseline reference is the first measurement obtained during the initial construction phase. Although (Truong-Hong *et al*. 2021) and references therein report different surface extraction schemes, advantages, limitations and their accuracies it can be inferred that differences in accuracy based on choice of method are minor, and do not have significant variation on small scale deformation. However, in the case of plastic

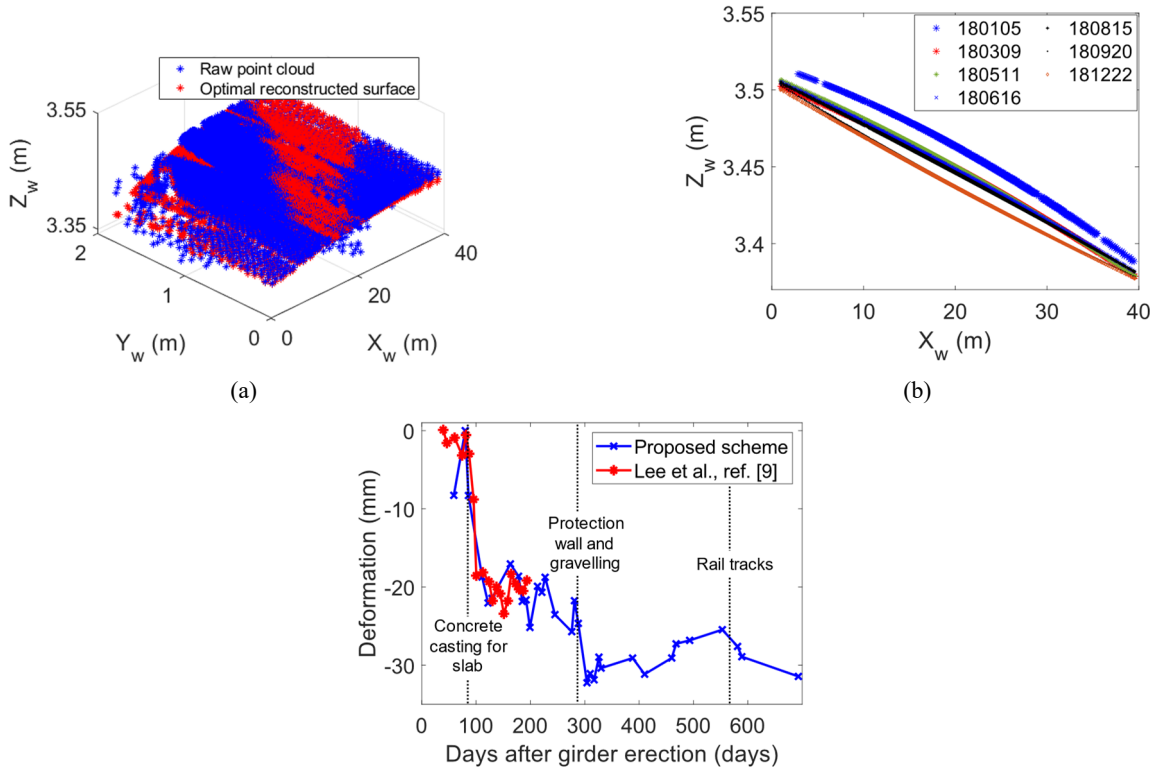

Fig. 12 (a) Optimal reconstructed shape using least squares-based shape sensing. (b) The reconstructed shape profile along mid-width involving different construction stages over a long duration for the full-scale bridge girder G1. (c) The long duration mid-span girder deflection (Numbers in the legend correspond to calendar dates in the format 'YYMMDD', where YY stands for the last two digits of the year, MM is the month, and DD is the date)

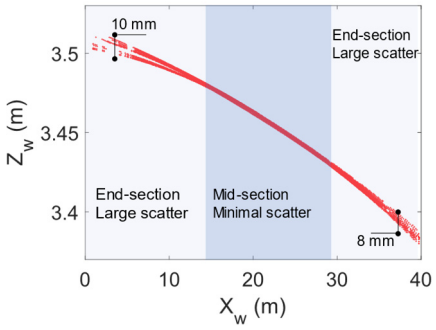

Fig. 13 Precision and accuracy error in the reconstructed deformation cross-section profile extracted along the span of the girder G1

deformation, surface fitting-based approaches are prone to have large deviations from ground truth. Insights from shape sensing include camber shape, which directly correlates with bridge safety. The girder construction was designed to have a curvature, assuming creep and stress relaxation during the concrete curing stage. The three major stages during the girder construction process are: concrete pouring, the addition of the protection wall and gravel, and placement of rail tracks. The addition of weight during each stage of construction induces additional deformation. The mid-span deflection of girder G1 measured using the proposed scheme closely matches the long-term displacement measurement of bridges using LiDAR (Lee *et al*. 2019), wherein additional retroreflectors are attached to the target structure for measurements. The details of ground truth measurement (Lee *et al*. 2019) are concisely discussed in Section 2. The proposed scheme eliminates the necessity of additional retroreflectors for measurements, which are not feasible to mount on a full-scale bridge girder under all circumstances.

The outputs from the proposed scheme have been quantitatively evaluated and compared to the ground truth measurement. The deformation quantity derived from shape sensing at the mid-point of the bridge girder from the proposed scheme was compared with state-of-the-art long-term deformation measurement (ground truth). The estimated magnitudes of deformation measurement were comparable and promising. The proposed scheme tracked the bridge's shape and deformation for 600 days, eliminating the need for continuously placing sensors on the field site for bridge girder monitoring.

Despite promising results for the long-term shape sensing of a full-scale bridge girder, it is noteworthy to discuss the associated measurement errors. The error in the reconstruction of the deformation profile along the span of the bridge girder is shown in Fig. 13. During the measurement, the laser scanner was placed approximately at the mid-span of the girder; hence, maximum accuracy and precision errors were observed at the end segments while minimum errors were observed at the mid-span. The range and orientation of the laser beam during the measurement increased towards the end segment; hence, the minimal spacing between the successive spatial measurement points increased at the end segment. These observations are in line with the findings on the influence of scanning parameters on point cloud data (Soudarissanane *et al*. 2011), which indicated that the precision of point cloud decreases with the incidence angle and range of measurement. Henceforth, measurements include lower weightage of point clouds at the extremes, contributing to significant variations in least squares-based shape sensing at the extremes. Often, lab-scale testing is performed at length scales that are far smaller than field-scale experiments. Measurements are often obtained within sweet spots or optimal limits. Hence, the observed precision and accuracy error for lab-scale measurements is minimal, whereas its effects are predominant during full-scale testing.

The computational time required for the proposed automated ROI extraction of the LiDAR point cloud was approximately 3 minutes. The point cloud data set has approximately one million points. The configuration of the computing platform are as follows: 10th Generation i9-10900f CPU with 10 cores, 20 threads, processor base frequency 2.8 GHz, 20 MB cache memory, 16 GB RAM, and a graphics card GTX 1660. The computing platform uses a Windows 10 operating system. Various hidden processing steps for the proposed automated ROI extraction include (i) loading the raw point cloud data sets of bridge girder and reference reflectors, cumulatively accounting for approximately one million points; (ii) preprocessing to eliminate non-stationary background, outlier extraction and removal, and ROI extraction of the girder and abutment in the LiDAR coordinate system; (iii) in-plane and out-of-plane transformation of point clouds to world coordinate system and (iv) least square based shape sensing.

4. Conclusions

This study presents a scheme for long-term shape sensing and deformation monitoring of full-scale bridge girder using point clouds with an automated extraction of ROI, invariant to LiDAR positions. The automated ROI extraction method efficiently removes background information, wherein 2D and 3D methods are combined along with the design model and pre-defined targets for ROI extraction. The pre-defined targets transforms the point clouds in the ROI from LiDAR coordinate system to unified world coordinate system. For example, the present approach uses four circular targets attached to abutments as pre-defined targets. The state-of-the-art 3D registration-based approaches for bridge girders fail to align the point clouds in a common reference frame due to local convergence, which is sensitive to the initial match configuration and often multiple manual iterations are required to achieve minimal errors. In contrast, the proposed approach consistently transforms the point clouds across multiple dimensions and coordinate systems, using both the 3D point cloud and 2D image spaces. The former uses advanced surface reconstruction schemes, whereas the latter uses Hough transform, edge detection, and corner extraction. The mathematical analysis of transforming the point clouds is detailed and the proposed scheme is validated on a full-scale bridge girder. Bridge deformation in the construction phase is further analysed using the reconstructed geometric model over a longer time period. Shape changes during the

construction phase are correlated with different loading stages. The developed approach considers (i) the complexities associated with the full-scale in situ smart construction of rail bridges (ii) data complexity in terms of volume and computation. The proposed methodology provides novel insights with significant applications in building information monitoring and in-process life-cycle analysis of precast concrete.

The limitations of the proposed study are as follows: (i) The proposed approach relies on subtracting consecutive surface-fitted point cloud datasets to monitor bridge girder deformation, making deformation a derived parameter from shape sensing. However, this approach cannot detect any localised stiffness change due to geometric and/or material property changes. The surface fitting scheme assumes that there are no stiffness/geometric changes locally. In the case of local non-uniform deformation, point clouds will be misinterpreted erroneously. Conversely, inaccurate point clouds obtained from imperfect construction can also give rise to inaccurate deformation. (ii) Although the planar resolution of the point cloud measurement is on a millimeter scale, the proposed approach cannot visualise the local variation in deformation. Point cloud measurement with sub-millimeter resolution requires triangulation scanners, which in practice limits the scanning speed and range of the measurement. (iii) The proposed approach for outlier removal used the z-coordinates of the point cloud and RANSAC method, which is modal-based and cannot eliminate the mixed pixel effect. By default, RANSAC assumes small-scale deformation, and in the present work, a small-scale bridge deformation is assumed within the deformation limit based on the design criteria; hence justifiable. This approach is applicable for the flat girder, where all points of the bottom surface are on the same elevation, while other girder types may require additional tweaking of the algorithm.

In the current work, the point clouds were acquired from a single scanning station, meaning that the range of point cloud measurement is confined to a smaller field of view. However, in bridge surveying, surveyors often employ multiple scanning stations, thereby accounting for a larger field of view. The ROI of the bridge girder under each field of view may have different elevations from ground level, curvature, and inclination. Therefore, future directions need to account for these effects in addition to stitching point clouds from different scanning stations. In the current research, as the span of the bridge girder was small, the authors had the opportunity to define and install pre-defined reference targets in the abutments. However, in the case of bridge girder with a large span, planar and/or vertical registration of point clouds from multiple scanning stations without pre-defined targets needs to be investigated. The non-target-based planar and/or vertical registration needs to rely on surface feature points in the ROI. The feasibility and efficacy need to be rigorously tested with respect to different field conditions.

Acknowledgments

The authors gratefully acknowledge financial support from a grant (NRF-2020R1A2C2014797) from the Basic Science Research Program through the National Research Foundation of Korea (NRF), funded by the Ministry of Education and National R&D Project for Smart Construction Technology (RS-2020-KA156887) funded by the Korea Agency for Infrastructure Technology Advancement under the Ministry of Land, Infrastructure and Transport and managed by the Korea Expressway Corporation.

References

Cabaleiro, M., Riveiro, B., Conde, B. and Sanchez-Rodriguez, A. (2020), "A case study of measurements of deformations due to different loads in pieces less than 1 m from lidar data", *Measurement*, **151**, 107196. https://doi.org/10.1016/j.measurement.2019.107196

Cha, G., Park, S. and Oh, T. (2019), "A terrestrial LiDAR-based detection of shape deformation for maintenance of bridge structures", *J. Constr. Eng. Manag.*, **145**(12), 04019075. https://doi.org/10.1061/(ASCE)CO.1943-7862.00017

Cha, G., Sim, S. H., Park, S. and Oh, T. (2020), "LiDAR-based bridge displacement estimation using 3D spatial optimization", *Sensors*, **20**(24), 7117. https://doi.org/10.3390/s20247117

Cho, S., Lee, J. and Sim, S.H. (2018), "Comparative study on displacement measurement sensors for high-speed railroad bridge", *Smart Struct. Syst., Int. J.*, **21**(5), 637-652. https://doi.org/10.12989/sss.2018.21.5.637

Colombani, I.A. and Andrawes, B. (2022), "A study of multi-target image-based displacement measurement approach for field testing of bridges", *J. Struct. Integr. Maint.*, **7**(4), 207-216. https://doi.org/10.1080/24705314.2022.2088071

Di-Stefano, F., Chiappini, S., Gorreja, A., Balestra, M. and Pierdicca, R. (2021), "Mobile 3D scan LiDAR: A literature review", *Geomat. Natural Hazards Risk*, **12**(1), 2387-2429. https://doi.org/10.1080/19475705.2021.1964617

Durrett, R. (2019), *Probability: Theory and Examples*, Vol. 49, Cambridge University Press.

Gharehbaghi, V.R., Kalbkhani, H., Noroozinejad Farsangi, E., Yang, T.Y., Nguyen, A., Mirjalili, S. and Málaga-Chuquitaype, C. (2022), "A novel approach for deterioration and damage identification in building structures based on Stockwell-Transform and deep convolutional neural network", *J. Struct. Integr. Maint.*, **7**(2), 136-150. https://doi.org/10.1080/24705314.2021.2018840

Girardeau-Montaut, D., Roux, M., Marc, R. and Thibault, G. (2005), "Change detection on points cloud data acquired with a ground laser scanner. International Archives of Photogrammetry", *Remote Sens. Spatial Inform. Sci.*, **36**(3).

Gordon, S.J. and Lichti, D.D. (2007), "Modeling terrestrial laser scanner data for precise structural deformation measurement", *J. Survey. Eng.*, **133**(2), 72-80. https://doi.org/10.1061/(ASCE)0733-9453(2007)133:2(72)

Graves, W., Aminfar, K. and Lattanzi, D. (2022), "Full-scale highway bridge deformation tracking via photogrammetry and remote sensing", *Remote Sensing*, **14**(12), 2767. https://doi.org/10.3390/rs14122767

Hough, P.V. (1962), U.S. Patent No. 3,069,654, Washington, DC: U.S. Patent and Trademark Office.

Hu, F., Zhao, J., Huang, Y. and Li, H. (2021), "Structure-aware 3D reconstruction for cable-stayed bridges: A learning-based method", *Comput.-Aided Civil Infrastr. Eng.*, **36**(1), 89-108. https://doi.org/10.1111/mice.12568

Kim, M.K., Sohn, H. and Chang, C.C. (2015), "Localization and quantification of concrete spalling defects using terrestrial laser

scanning", *J. Comput. Civil Eng.*, **29**(6), 04014086. https://doi.org/10.1061/(ASCE)CP.1943-5487.00004

Kim, M.K., Wang, Q., Park, J.W., Cheng, J.C., Sohn, H. and Chang, C.C. (2016), "Automated dimensional quality assurance of full-scale precast concrete elements using laser scanning and BIM", *Automat. Constr.*, **72**, 102-114. https://doi.org/10.1016/j.autcon.2016.08.035

Kim, H., Yoon, J. and Sim, S.H. (2020), "Automated bridge component recognition from point clouds using deep learning", *Struct. Control Health Monitor.*, **27**(9), e2591. https://doi.org/10.1002/stc.2591

Kim, H., Lee, S., Ahn, E., Shin, M. and Sim, S.H. (2021a), "Crack identification method for concrete structures considering angle of view using RGB-D camera-based sensor fusion", *Struct. Health Monitor.*, **20**(2), 500-512. https://doi.org/10.1177/1475921720934758

Kim, H., Yoon, J., Hong, J. and Sim, S.H. (2021b), "Automated damage localization and quantification in concrete bridges using point cloud-based surface-fitting strategy", *J. Comput. Civil Eng.*, **35**(6), 04021028. https://doi.org/10.1061/(ASCE)CP.1943-5487.00009

Kolappan Geetha, K. and Sim, S.H. (2022), "Fast identification of concrete cracks using 1D deep learning and explainable artificial intelligence-based analysis", *Automat. Constr.*, **143**, 104572. https://doi.org/10.1016/j.autcon.2022.104572

Kolappan Geetha, G., Yang, H.J. and Sim, S.H. (2023), "Fast detection of missing thin propagating cracks during deep-learning-based concrete crack/non-crack classification", *Sensors*, **23**(3), 1419, https://doi.org/10.3390/s23031419

Lague, D., Brodu, N. and Leroux, J. (2013), "Accurate 3D comparison of complex topography with terrestrial laser scanner: Application to the Rangitikei canyon (NZ)", *ISPRS J. Photogramm. Remote Sens.*, **82**, 10-26. https://doi.org/10.1016/j.isprsjprs.2013.04.009

Lee, J., Lee, K.C., Cho, S. and Sim, S.H. (2017), "Computer vision-based structural displacement measurement robust to light-induced image degradation for in-service bridges", *Sensors*, **17**(10), 2317. https://doi.org/10.3390/s17102317

Lee, J., Lee, K.C., Lee, S., Lee, Y.J. and Sim, S.H. (2019), "Long-term displacement measurement of bridges using a LiDAR system", *Struct. Control Health Monitor.*, **26**(10), e2428. https://doi.org/10.1002/stc.2428

Lee, J., Lee, K.C., Jeong, S., Lee, Y.J. and Sim, S.H. (2020a), "Long-term displacement measurement of full-scale bridges using camera ego-motion compensation", *Mech. Syst. Signal Process.*, **140**, 106651. https://doi.org/10.1016/j.ymssp.2020.106651

Lee, S., Lee, J., Park, J.W. and Sim, S.H. (2020b), "Nontarget-based measurement of 6-DOF structural displacement using combined RGB color and depth information", *IEEE/ASME Transact. Mechatron.*, **26**(3), 1358-1368. https://doi.org/10.1109/TMECH.2020.3019288

Lee, J.S., Park, J. and Ryu, Y.M. (2021), "Semantic segmentation of bridge components based on hierarchical point cloud model", *Automat. Constr.*, **130**, 103847. https://doi.org/10.1016/j.autcon.2021.103847

Li, Y., Ma, L. Zhong, Z., Liu, F., Cao, D., Li, J. and Chapman, M.A. (2020), "Deep learning for lidar point clouds in autonomous driving: A review", *IEEE Trans. Neural Networks Learn. Syst.*, **32**(8), 3412-3432. https://doi.org/10.48550/arXiv.2005.09830

Liu, M., Sun, X., Wang, Y., Shao, Y. and You, Y. (2020), "Deformation measurement of highway bridge head based on mobile TLS data", *IEEE Access*, **8**, 85605-85615. https://doi.org/10.1109/ACCESS.2020.2992590

Lu, R., Brilakis, I. and Middleton, C.R. (2019), "Detection of structural components in point clouds of existing RC bridges", *Comput.-Aided Civil Infrastr. Eng.*, **34**(3), 191-212. https://doi.org/10.1111/mice.12407

Melo, A.G., Pinto, M.F., Honorio, L.M., Dias, F.M. and Masson, J.E. (2020), "3D correspondence and point projection method for structures deformation analysis", *IEEE Access*, **8**, 177823-177836. 10.1109/ACCESS.2020.3027205

Napolitano, R., Liu, Z., Sun, C. and Glisic, B. (2019), "Combination of image-based documentation and augmented reality for structural health monitoring and building pathology", *Front. Built Environ.*, **5**, 50. https://doi.org/10.3389/fbuil.2019.00050

Ng, H.F., Jargalsaikhan, D., Tsai, H.C. and Lin, C.Y. (2013), "An improved method for image thresholding based on the valley-emphasis method", In: *Asia-Pacific Signal and Information Processing Association Annual Summit and Conference IEEE*, pp. 1-4. https://doi.org/10.1109/APSIPA.2013.6694261

Nocerino, E., Stathopoulou, E.K., Rigon, S. and Remondino, F. (2020), "Surface reconstruction assessment in photogrammetric applications", *Sensors*, **20**(20), 5863. https://doi.org/10.3390/s20205863

Oskouie, P., Becerik-Gerber, B. and Soibelman, L. (2016), "Automated measurement of highway retaining wall displacements using terrestrial laser scanners", *Automat. Constr.*, **65**, 86-101. https://doi.org/10.1016/j.autcon.2015.12.023

Otsu, N. (1979), "A threshold selection method from gray-level histograms", *IEEE Transact. Syst. Man Cybernet.*, **9**(1), 62-66. https://doi.org/10.1109/TSMC.1979.4310076

Pan, Y., Dong, Y., Wang, D., Chen, A. and Ye, Z. (2019), "Three-dimensional reconstruction of structural surface model of heritage bridges using UAV-based photogrammetric point clouds", *Remote Sensing*, **11**(10), 1204. https://doi.org/10.3390/rs11101204

Park, H.S., Lee, H.M., Adeli, H. and Lee, I. (2007), "A new approach for health monitoring of structures: terrestrial laser scanning", *Comput.-Aided Civil Infrastr. Eng.*, **22**(1), 19-30. https://doi.org/10.1111/j.1467-8667.2006.00466.x

Royo, S. and Ballesta-Garcia, M. (2019), "An overview of lidar imaging systems for autonomous vehicles", *Appl. Sci.*, **9**(19), 4093. https://doi.org/10.3390/app9194093

Rutzinger, M., Rottensteiner, F. and Pfeifer, N. (2009), "A comparison of evaluation techniques for building extraction from airborne laser scanning", *IEEE J. Select. Topics Appl. Earth Observ. Remote Sensing*, **2**(1), 11-20. https://doi.org/10.1109/JSTARS.2009.2012488

Schnabel, R., Wahl, R. and Klein, R. (2007), "Efficient RANSAC for point-cloud shape detection", In: *Computer Graphics Forum*, Oxford, UK: Blackwell Publishing Ltd., **26**(2), pp. 214-226. https://doi.org/10.1111/j.1467-8659.2007.01016.x

Sohn, H. and Park, B. (2021), "Laser-based structural health monitoring", In: Beer, M., Kougioumtzoglou, I., Patelli, E., Au, IK. (eds) *Encyclopedia of Earthquake Engineering*, Springer, Berlin, Heidelberg. https://doi.org/10.1007/978-3-642-36197-5_86-1

Soudarissanane, S., Lindenbergh, R., Menenti, M. and Teunissen, P. (2011), "Scanning geometry: Influencing factor on the quality of terrestrial laser scanning points", *ISPRS J. Photogramm. Remote Sens.*, **66**(4), 389-399. https://doi.org/10.1016/j.isprsjprs.2011.01.005

Strang, G. (2022), *Introduction to Linear Algebra*, Wellesley-Cambridge Press.

Tan, K. and Cheng, X. (2016a), "Correction of incidence angle and distance effects on TLS intensity data based on reference targets", *Remote Sensing*, **8**(3), 251. https://doi.org/10.3390/rs8030251

Tan, K. and Cheng, X. (2016b), "Surface reflectance retrieval from the intensity data of a terrestrial laser scanner", *JOSA A*, **33**(4),

771-778. https://doi.org/10.1364/JOSAA.33.000771
Tan, K., Chen, J., Qian, W., Zhang, W., Shen, F. and Cheng, X. (2019), "Intensity data correction for long-range terrestrial laser scanners: A case study of target differentiation in an intertidal zone", *Remote Sensing*, **11**(3), 331. https://doi.org/10.3390/rs11030331
Torr, P.H. and Zisserman, A. (2000), "MLESAC: A new robust estimator with application to estimating image geometry", *Comput. Vision Image Understand.*, **78**(1), 138-156. https://doi.org/10.1006/cviu.1999.0832
Truong, M.T.N. and Kim, S (2018), "Automatic image thresholding using Otsu's method and entropy weighting scheme for surface defect detection", *Soft Computat.*, **22**, 4197-4203. https://doi.org/10.1007/s00500-017-2709-1
Truong-Hong, L. and Lindenbergh, R. (2019), "Measuring deformation of bridge structures using laser scanning data", In: *4th Joint International Symposium on Deformation Monitoring* (*JISDM*), p. 7.
Truong-Hong, L. and Lindenbergh, R. (2022), "Automatically extracting surfaces of reinforced concrete bridges from terrestrial laser scanning point clouds", *Automat. Constr.*, **135**, 104127. https://doi.org/10.1016/j.autcon.2021.104127
Truong-Hong, L., Lindenbergh, R. and Nguyen, T.A. (2021), "Structural assessment using terrestrial laser scanning point clouds", *Int. J. Build. Pathol. Adaptat.*, **40**(3), 345-379.
Wang, Z. and Menenti, M. (2021), "Challenges and opportunities in Lidar remote sensing", *Front. Remote Sens.*, **2**, p. 3. https://doi.org/10.3389/frsen.2021.641723
Wang, K., Ma, S., Chen, J., Ren, F. and Lu, J. (2020), "Approaches, challenges, and applications for deep visual odometry: Toward complicated and emerging areas", *IEEE Transact. Cognit. Develop. Syst.*, **14**(1), 35-49. https://doi.org/10.1109/TCDS.2020.3038898
Xia, T., Yang, J. and Chen, L. (2022), "Automated semantic segmentation of bridge point cloud based on local descriptor and machine learning", *Automat. Constr.*, **133**, 103992. https://doi.org/10.1016/j.autcon.2021.103992
Xu, Y. and Stilla, U. (2021), "Towards building and civil infrastructure reconstruction from point clouds: A review on data and key techniques", *IEEE J. Select. Topics Appl. Earth Observ. Remote Sens.*, **14**, 2857-2885. https://doi.org/10.1109/JSTARS.2021.3060568
Yan, Y. and Hajjar, J.F. (2021), "Automated extraction of structural elements in steel girder bridges from laser point clouds", *Automat. Constr.*, **125**, 103582. https://doi.org/10.1016/j.autcon.2021.103582
Yang, T., Li, Y., Zhao, C., Yao, D., Chen, G., Sun, L., Krajnik, and T. and Yanet, Z. (2022), "3D ToF LiDAR in mobile robotics: A review", arXiv Prepr, arXiv2202.11025. https://doi.org/10.48550/arXiv.2202.11025
Ye, C., Acikgoz, S., Pendrigh, S., Riley, E. and DeJong, M.J. (2018), "Mapping deformations and inferring movements of masonry arch bridges using point cloud data", *Eng. Struct.*, **173**, 530-545. https://doi.org/10.1016/j.engstruct.2018.06.094
Ziolkowski, P., Szulwic, J. and Miskiewicz, M. (2018), "Deformation analysis of a composite bridge during proof loading using point cloud processing", *Sensors*, **18**(12), 4332. https://doi.org/10.3390/s18124332